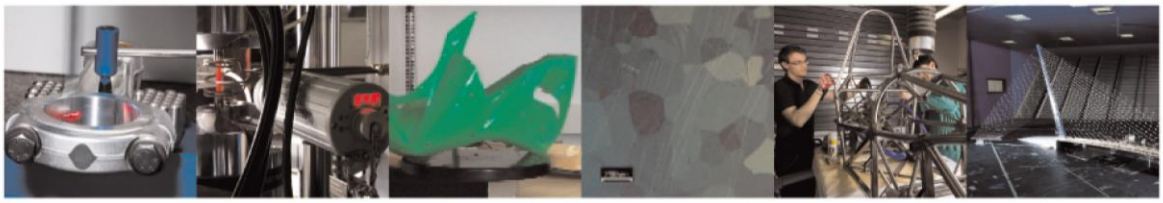

Prescriptive Data-Analytical Modeling of Laser Powder Bed Fusion Processes for Accuracy Improvement

Luan, He; Grasso, Marco; Colosimo, Bianca M.; Huang, Qiang

This is a post-peer-review, pre-copyedit version of an article published in JOURNAL OF MANUFACTURING SCIENCE AND ENGINEERING, 141/1, on November 8, 2018. The final authenticated version is available online at: http://dx.doi.org/10.1115/1.4041709

https://asmedigitalcollection.asme.org/manufacturingscience/article/doi/10.1115/1.4041709/367176/Prescriptive-DataAnalytical-Modeling-of-Laser

DIPARTIMENTO DI MECCANICA ■ POLITECNICO DI MILANO
via G. La Masa, 1 ■ 20156 Milano ■ EMAIL (PEC): pecmecc@cert.polimi.it
http://www.mecc.polimi.it
Rev. 0

Prescriptive Data-Analytical Modeling of Laser Power Bed Melting Processes for Accuracy Improvement

He Luan[1], Marco Grasso[2], Bianca M. Colosimo[2], and Qiang Huang[1]

[1]Epstein Department of Industrial and Systems Engineering,
University of Southern California, Los Angeles, CA, 90089, USA
[2]Department of Mechanical Engineering,
Politecnico di Milano, 20156, Milano, Italy

Abstract

Laser Power Bed Fusion (LPBF) has the ability to produce three-dimensional (3D) lightweight metal parts with complex shapes. Extensive investigations have been conducted to tackle build accuracy problems caused by shape complexity. For metal parts with stringent requirements, surface roughness, laser beam positioning error, and part location effect can all affect the shape accuracy of LPBF built products. This study develops a data-driven predictive approach as a promising solution for geometric accuracy improvement in LPBF processes. To address the shape complexity issue, a prescriptive modeling approach is adopted to minimize geometrical deviations of built products through compensating CAD models, as opposed to changing process parameters. It allows us to predict and control a wide range of shapes starting from a limited set of measurements on basic benchmark geometries. An error decomposition and compensation scheme is developed to decouple the influence from different error components and to reduce the shape deviations caused by part geometrical deviation, laser beam positioning error and other location effects simultaneously via an integrated modeling and compensation framework. Experimentation and data collection are conducted to investigate error sources and to validate the developed modeling and accuracy control methods.

1 Introduction

The metal Additive Manufacturing (AM) market has been growing at double-digit rates in recent years [1]. Among various technologies suitable to produce metal parts on a layer-by-layer basis, Laser Power Bed Fusion (LPBF) uses laser to locally melt fine metal powder along pre-defined scanning paths [2]. It has the capability to produce parts with customized complex shapes and desired mechanical properties. Despite successful demonstrations in highly regulated aerospace and healthcare sectors, LPBF faces quality issues such as geometric distortions, surface defects, poor dimensional accuracy, porosity, residual stresses, cracks and delamination, balling phenomena, microstructural inhomogeneities and impurities. Comprehensive reviews of these defects, including their root causes and final impacts on part quality and mechanical properties can be found in [3–9].

Dimensional and geometric deviations in LPBF can be further classified into: i) shrinkage and oversize effects, ii) warping, curling and other geometrical distortions, iii) dross formation at down-facing surfaces, and iv) super-elevated edges. To address these issues, efforts have been devoted to relating the energy input from the laser source to the fusion of materials and understanding the effects of laser-material interactions on build quality for optimal selection of process settings and scanning strategies (please refer to [5] and references therein). Indeed, process parameters determine the melt pool size and stability, which affect not only part microstructures, but also track geometries, and consequently the shapes and dimensions of the end-part. For example, part shrinkage and over-size effects in LPBF are observed and investigated in [10–12].

In addition, proper optical system alignment, mirror quality, perfection of the $f-\theta$ lens, and the uniformity of laser beam profile across the build area have been attributed to in-plane geometrical accuracy as well [13]. The study in [14] points out that a mis-calibrated system may result in parts with inaccurate final dimensions. An elliptical distortion of the laser spot in LPBF may occur near the edges of the baseplate due to high scanner deflection angles, which inflates the local dimensional and geometrical inaccuracy, depending on the

part location on the baseplate [14].

Warping effects are believed to be influenced by heat dissipation mechanisms and the development of thermal stresses during the build [11]. Non-uniform thermal expansion and part contraction lead to the so-called curling phenomenon [2]. The study in [15] shows that this phenomenon is usually associated with an uneven shrinkage between the top and the bottom of overhanging areas. A combination of shrinking and warping effects yield curved profiles of down-facing surfaces intended to be flat. Thermal stress-induced distortions can be mitigated by pre-heating the base plate [16], a procedure commonly adopted by industrial LPBF systems to avoid abrupt temperature changes between successive layers for alleviating thermal stresses. An alternative solution adapts process parameters to the local geometries and sizes of the part [11]. In the presence of down-facing surfaces, dross formation and bad contours are known to be caused by a lack or an improper design of supporting structures [17]. The study in [17] proposes a feedback control method to reduce surface roughness by adjusting laser power based on in-situ melt pool measurement.

Super-elevated edge represents another type of out-of-plane geometrical distortion, featured by elevated ridges of the solidified material. It not only affects end-part quality, but also induces the propagation of defects due to possible interferences with the powder recoating system. The work in [18] discusses the effect of process parameters and scanning strategies on the flatness of scanned surfaces and the generation of super-elevated edges.

Despite a wide literature devoted to the study of the final part quality and the factors that affect the process accuracy, currently a comprehensive causal model is hard to be established due the process complexity. A data-driven predictive approach is therefore a promising alternative to improve the geometric accuracy for LPBF processes. We aim to contribute to the LPBF literature from two aspects. First, we propose a data-analytical modeling approach that allows us to minimize geometrical deviations through compensating CAD models rather than varying the process parameters. Second, the proposed modeling approach is prescriptive in the sense that it allows us to predict and control the geometric deviations of arbitrary

shapes starting from a limited set of measurements on basic benchmark geometries. The proposed modeling approach applies to in-plane geometric and dimensional deviations.

Our prescriptive modeling approach is based on the in-plane shape deviation modeling and compensation strategies established in a series of works for AM built products [19–27]. Methodology validation has been conducted and successfully demonstrated in the stereolithography (SLA) processes not only for simple shapes such as cylinders [19] or polyhedrons [21], but also for arbitrary freeform shapes [27]. The strategy has also been extended to fused deposition modeling (FDM) processes [28, 29] and out-of-plane geometric modeling [30–32]. However, extending the existing approach to LPBF processes faces new challenges:

- *Surface roughness coupled with shape deviation profile*: When LPBF built parts are small in size, the shape deviation error may be comparable in magnitude to the surface roughness, causing large uncertainty in the determination of the actual shape profile.

- *Laser beam positioning error*: Unlike the projection based AM processes, the position accuracy of laser beam in LPBF (and other laser based AM processes) may vary with location, leading to location-dependent positioning error.

- *Additional machine-dependent local effects*: further location-dependent effects on the shape deviation profile may be introduced by specific properties of the LPBF system used to fabricate the part. They can be caused by non-uniform inert gas flow within the building chamber or other inaccuracies of the equipment used for chamber environmental control. For example, non-laminar gas flow may cause input energy attenuation, gas entrapment, spatter contamination, etc. Please refer to [33, 34] for details.

We propose an integrated experimental and modeling approach to improve the in-plane geometrical part quality in LPBF processes by addressing these new issues due to surface roughness, laser beam positioning error, and other location effects.

Following the introduction, our proposed strategy of prescriptive in-plane ($x-y$ plane) shape deviation modeling in LPBF processes will first be formulated in Section 2. Section 3 illustrates the prescriptive in-plane shape deviation modeling for arbitrary shapes considering surface roughness. Section 4 and Section 5 introduce the analysis and prediction method for laser beam positioning error and machine-dependent location effects, respectively. A final summary and conclusion is given in Section 6.

2 Proposed Strategy

Our goal is to improve the geometrical accuracy by reducing shape deviations. Issues arising from LPBF such as surface roughness, laser beam positioning error, and other location effects, have not been considered in [19, 21, 24, 27].

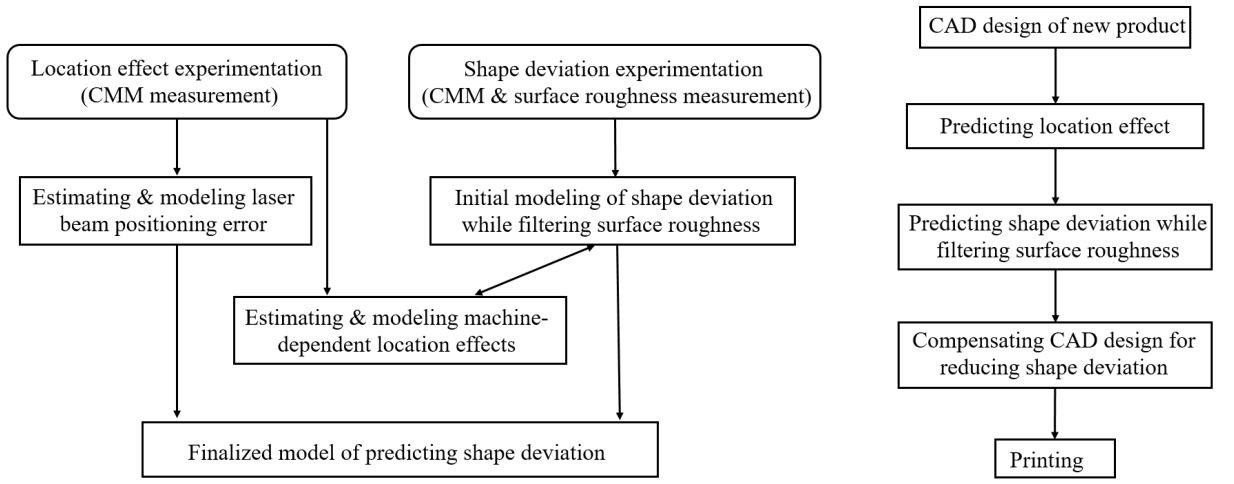

(a) *Modeling procedure* **(b)** *Implementation procedure*

Figure 1: *Flow chart of proposed strategy for accuracy improvement*

To fill the gap and establish a data-analytical approach for LPBF processes, we propose in Fig. 1a a modeling procedures based on LPBF experimentation. Two sets of experiments are required: (1) location effect experimentation for investigating the laser beam positioning error and other location effects; and (2) shape deviation experimentation for establishing shape deviation models. Metrology effort includes surface roughness measurement and CMM

(coordinate measurement machine) measurement of geometrical shapes.

This modeling procedure involves three components:

- *Prescriptive shape deviation modeling for freeform shapes in LPBF processes considering surface roughness*: The actual measured deviation of product boundary is denoted by $\Delta r(\theta)$. (Please see details in Section 3.2). It can be represented as: $\Delta r(\theta) = f(\cdot)+\epsilon_\theta$, where θ is the location angle under the Polar Coordinate System (PCS), $\Delta_r(\theta)$ is the shape deviation along radius direction at angle θ, $f(\cdot)$ is the shape deviation model, and error term $\epsilon_\theta \sim N(0, \sigma^2)$. The prescriptive model $f(\cdot)$ will be initially established with a few test cases from shape deviation experiments (Fig. 1a). To filter out the influence of surface roughness and achieve better prediction of shape deviations, we split the variance of error term into $\sigma^2 = \sigma_1^2 + \sigma_2^2$ where σ_1^2 and σ_2^2 are related to shape deviations and surface roughness, respectively. The surface roughness related term σ_2 will be measured and assumed to be consistent among shapes, while σ_1 has to be estimated.

- *Laser beam positioning error modeling using error equivalence concept*: Similar to FDM extruders [28, 29], laser beam during printing process may deviate from its intended position (x, y) by error $(e_x(x, y), e_y(x, y))$. To predict the laser beam positioning errors, we adopt the error equivalence concept [35–38], by transforming the positioning error into the equivalent amount of shape design error. One simple illustrate of the error equivalence concept is that a design error that leads to the increased size or boundary of a product can be replicated by moving the laser position. The outcomes of the two different error sources are equivalent and one can be chosen to represented the other. The transformed positioning error will be readily integrated into the shape deviation prediction model, which will simplify the model building and compensation. Note that only the fixed effect of laser beam positioning error is considered. Random and time-varying effects of the laser beam positioning error are not captured by the model.

- *Location effect modeling to capture other machine-related location effects*: The machine-dependent location effect is approximated as a fixed effect at each location to affect build accuracy. Following the same logic, we adopt the error equivalence concept and use a location-dependent term $x_0(s)$ to capture the machine-dependent location effect at location s. Termed as the *location effect term*, it is represented as the equivalent amount of shape design error as well, which can be easily integrated into the finalized shape prediction model. Similar treatment can be found for "over-exposure" effect in SLA processes [19]. Again, like the laser beam positioning error, only the fixed effect of location effect is considered.

Once the shape deviation model is established, accuracy prediction and compensation before printing a new part can follow the procedure in Fig. 1b.

3 Prescriptive Shape Deviation Modeling for Freeform Shapes in LPBF with Surface Roughness Influence

3.1 Shape Deviation Experimentation for LPBF

The design of shape deviation experimentation is shown in Fig. 2. All six test parts are produced on the same baseplate by using a Renishaw AM250 LPBF system. Among them, three cylinders (or circular disks), one square disk and one pentagon disk are adopted as training samples for model building. The freeform shape is used to test the prescriptive power of the established model, i.e., using only a few simple test parts (five in our study) to predict shape deviation of freeform products.

A gas-atomized 18Ni (300) maraging alloy powder supplied by Sandvik Osprey LTD (Neath, UK) with average particle size of $35\mu m$ is used. Default process parameters for this metal powder type are shown in Table 1. Point distance d_p represents the distance between successive laser exposure points along one scan line, while meandering scan strategy adopts

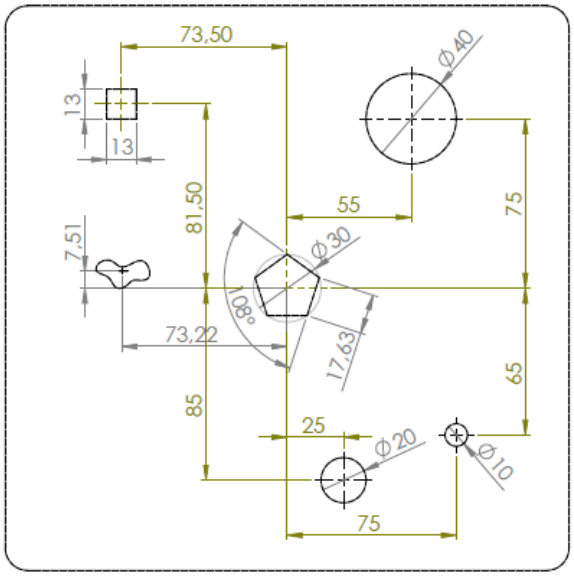

Figure 2: *Design of shape deviation experimentation on a single plate (unit: mm)*

parallel scan tracks with opposite scanning directions between tracks.

The height of all the parts is 5mm. The shape profile measurements for in-plane error evaluation are performed at a fixed height of 4.5mm above the baseplate by using a Zeiss Prismo 5 VAST MPS HTG Coordinate Measuring Machine (CMM) equipped with a 1mm radius probe.

Table 1: *The specific parameters of the LPBF process*

Variable	value
laser power P	$200W$
exposure time t	$104\mu s$
point distance along the track d_p	$65\mu m$
hatch distance d_h	$80\mu m$
layer thickness z	$50\mu m$
scanning strategy	meandering

3.2 Initial Analysis of Shape Deviations In LPBF Process

The CMM measurement of test parts provides point coordinates of part boundaries defined in the Cartesian Coordinate System (CCS). Following [19], the coordinates (x, y) (in-plane shape) in the CCS will be transformed into (r, θ) in the PCS. Comparing to nominal design

shapes, part shape deviation in the PCS is denoted as $\Delta r(\theta)$. As pointed out in [19], the advantage of this representation is the decoupling of modeling and shape complexity.

Figure 3 illustrates the deviation profiles $\Delta r(\theta)$ (red dots) of three circular disks with radii $20mm$, $10mm$ and $5mm$.

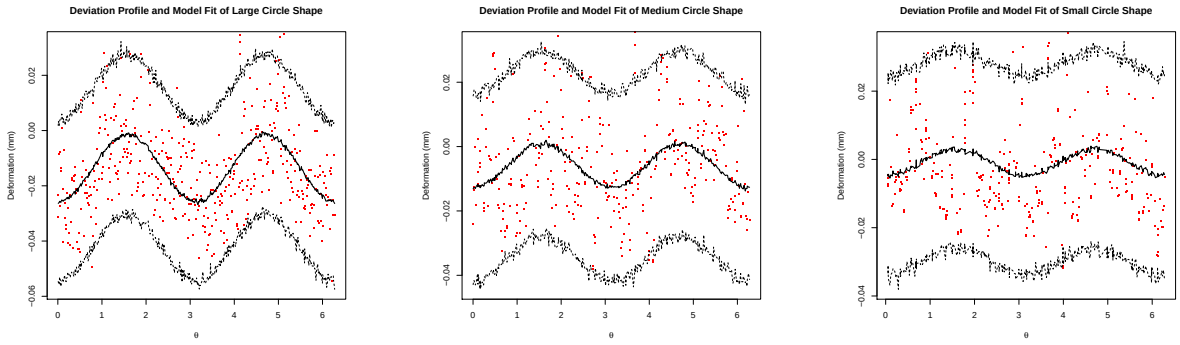

(a) $20mm$ *cylinder* **(b)** $10mm$ *cylinder* **(c)** $5mm$ *cylinder*

Figure 3: *Deviation (dots) and prediction profiles (solid lines denote posterior means, and dashed lines denote the* 2.5% *and* 97.5% *posterior quantiles) of three cylinders by cylindrical basis model* g_1

The shape deviation profiles $\Delta r(\theta)$ (red dots) of the square and pentagon disks with circumcircle radii $13\sqrt{2}mm$ and $15mm$ are shown in Fig. 4.

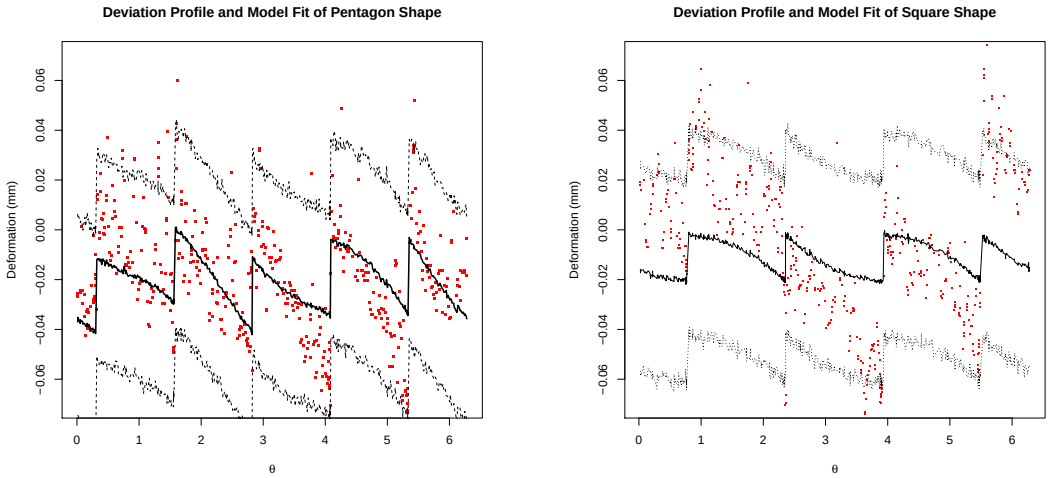

(a) $15mm$ *pentagon* **(b)** $13\sqrt{2}mm$ *square*

Figure 4: *Deviation (dots) and prediction profiles (solid lines denote posterior means, and dashed lines denote the* 2.5% *and* 97.5% *posterior quantiles) of the polyhedron shapes by freeform model*

Since our goal is to establish one model for predicting the shape deviations of different

shapes, Huang et al. (2014) [21] devises a cookie-cutter modeling framework to connect different shapes and [27] extends by formulating a prescriptive shape deviation model for freeform shapes as Eq. 1:

$$\Delta r(\theta, r(\theta)) = g_1(\theta, r(\theta)) + g_2(\theta, r(\theta)) + \epsilon_\theta \tag{1}$$

where basis function g_1 represents the deviation pattern of cylindrical shape or circular sectors of a cylinder, and basis g_2 is the cookie-cutter function that carves the others shapes from the cylindrical base. g_2 is particularly necessary if there are straight edges and corners.

The cylindrical shape is considered as the fundamental model building block (Note that in the study of in-plane shape deviations, the cylindrical disks are treated as 2D shapes or circles). One example of cylinder deviation model g_1 for SLA processes is given by Eq. 2 [19].

$$g_1(\theta, r_0) = x_0 + \beta_0(r_0 + x_0)^a + \beta_1(r_0 + x_0)^b \cos(2\theta) \tag{2}$$

where x_0 is a constant shape-independent effect (e.g., light over-exposure) underlying the SLA process, r_0 is the nominal radius of the circumcircle, θ is the angular position, while β_0, β_1, a and b are coefficients that have to be estimated.

Bayesian estimation of the model parameters in Eq. 2 can be conducted through Markov Chain Monte Carlo (MCMC) [19]. Using the data of three circular disks in our experiment (Fig. 3), the estimated model parameters of $g_1(\cdot)$ are given in Table 2. The prediction profiles and their confidence interval are shown in Fig. 3 as well. Note that we assume the priors $a \sim N(1, 2^2)$, $b \sim N(1, 1^2)$, $\log(x_0) \sim N(0, 1^2)$ and place flat priors on β_0, β_1, and $\log(\sigma)$.

The cookie-cutter function g_2 connects the cylindrical shape model to polygons by treating a polygon as being cut from its circumcircle [20, 21]. One example is the sawtooth wave function as Eq. 3.

Table 2: *Summary of posterior draws in cylindrical basis model*

	Mean	SD	2.5%	Median	97.5%
β_0	-0.003623	0.001137	-0.005463	-0.003824	-0.001186
β_1	-0.001065	4.3919×10^{-4}	-0.002040	-0.001018	-0.000339
a	0.626926	0.104855	0.4950065	0.597999	0.915121
b	0.841573	0.157791	0.5731525	0.831657	1.202621
x_0	0.008658	0.002045	0.004202	0.009035	0.012160
σ	0.014855	3.0791×10^{-4}	0.014281	0.014861	0.015475

$$g_2(\theta, r_0) = \beta_2(r_0 + x_0)^{\alpha} saw.tooth(\theta - \phi_0) = \beta_2(r_0 + x_0)^{\alpha}(\theta - \phi_0) MOD(\frac{2\pi}{n}) \tag{3}$$

where ϕ_0 is a phase variable determined by the smallest angular distance from the vertex of a polygon to the axis of the PCS, n is the number of polygon sides, $x\ MOD\ y =$ remainder of (x/y), while β_2, α are coefficients to be estimated.

We pool the data of square and pentagon disks (Fig. 4) together with three circular disks to estimate the complete freeform model Eq. 1. To specify a model robust to both cylinder and polygon shapes, we keep the parameters a, b and x_0 in Table 2. The parameter estimation with same Bayesian procedure as well as the prediction profiles are given in Table 3 and Figure 4. We assume prior $\alpha \sim N(1, 1^2)$ and place flat priors on β_0, β_1, β_2, and $\log(\sigma)$.

Table 3: *Summary of posterior draws for estimating freeform model*

	Mean	SD	2.5%	Median	97.5%
β_0	-0.002653	1.1062×10^{-4}	-0.002861	-0.002651	-0.002444
β_1	-6.9131×10^{-4}	7.4398×10^{-5}	-8.3113×10^{-4}	-6.9054×10^{-4}	-5.4787×10^{-4}
β_2	-5.5581×10^{-4}	2.7009×10^{-4}	-0.001174	-5.2043×10^{-4}	-1.1727×10^{-4}
α	1.436602	0.212887	1.088236	1.415376	1.998083
σ	0.020724	3.3094×10^{-4}	0.020086	0.020726	0.021376

The work in [26,27] further extends the framework to freeform shape by generalizing the basis functions g_1 and g_2 with the proposed Circular Approximation with Selective Cornering (CASC) strategy. In CASC strategy, a n-side polygon (n is large) first approximates the freeform shape. Then a series of sectors approximate the polygon. Equation 2 is extended

to Eq. 4 by applying cylindrical base model to each sector with different nominal radius.

$$g_1(\theta, r(\theta)) = x_0 + \beta_0(r_i(\theta_i) + x_0)^a + \beta_1(r_i(\theta_i) + x_0)^b \cos(2\theta) \quad for \;\; \theta_{i-1} \leq \theta < \theta_i, \;\; 1 \leq i \leq n, \;\; \theta_0 = \theta_n \quad (4)$$

where θ_i $(1 \leq i \leq n)$ is the position of each approximated vertex and $r_i(\theta_i)$ $(1 \leq i \leq n)$ is the nominal radius of each approximated sector

Equation 3 is generalized as Eq. 5 based on the observation that only vertices with sharp transitions in the approximated polygon will be selected for the cookie-cutter function to alternate the function amplitude.

$$g_2(\theta, r(\theta)) = \beta_2(r_j(\theta_j) + x_0)^\alpha saw.tooth(\theta) = \begin{cases} \beta_2(r_j(\theta_j) + x_0)^\alpha \dfrac{\pi(\theta - \theta_{j-1}) \text{ MOD } (\theta_j - \theta_{j-1})}{2(\theta_j - \theta_{j-1})} \\ \quad if \;\; \theta_{j-1} \leq \theta < \theta_j, \;\; 1 \leq j \leq n, \;\; \theta_0 = \theta_n, \\ \quad\quad \theta_j = \vartheta_k, \;\; 1 \leq k \leq m \\ 0, \;\; otherwise \end{cases} \quad (5)$$

where m is the number of selected vertices for the cookie-cutter function with $m \ll n$, and ϑ_k, $k = 1, 2, ..., m$ is the angle of m vertices. For further details, the interested readers can refer to [27].

Applying the estimated parameters to the generalized freeform model (Eqs. 1, 4 and 5), we derive the prediction profile of the freeform with circumcircle radius $12mm$ in Figure 6. Here circumcircle means the smallest circle that contains the freeform shape.

The prediction results capture the main trend of shape deviation well. However, since the relatively small size of experimental parts leads to small shape deviation, it is necessary to verify whether the actual geometric deviation is significant in the test parts. The null hypothesis is that there is no geometric shape deviation in the 6 experimental parts (Figure

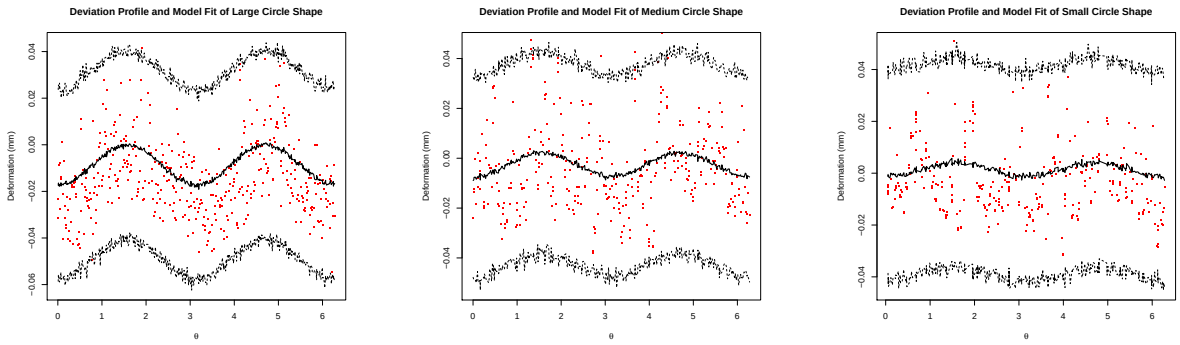

(a) $20mm$ *cylinder* **(b)** $10mm$ *cylinder* **(c)** $5mm$ *cylinder*

Figure 5: *Deviation (dots) and prediction profiles (solid lines denote posterior means, and dashed lines denote the* 2.5% *and* 97.5% *posterior quantiles) of three cylinders by freeform model*

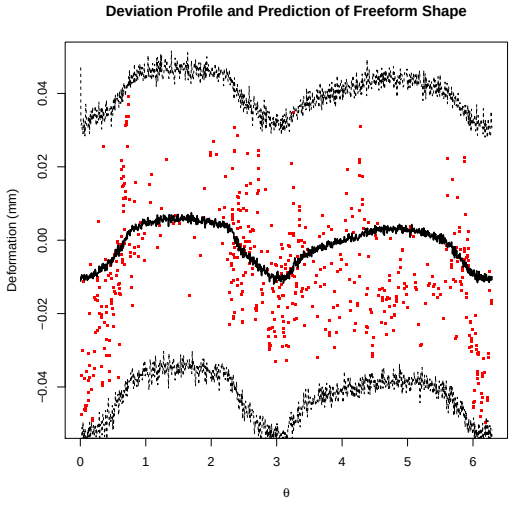

Figure 6: *Deviation profile (dots) and prediction (solid lines denote posterior means, and dashed lines denote the* 2.5% *and* 97.5% *posterior quantiles) of* $12mm$ *freeform shape*

2), the Bayesian posterior intervals are used. Figures 5, 4 and 6 indicate 95% predictive intervals that contain the zero line, meaning the null hypothesis cannot be rejected.

A major reason of this conclusion is the low signal to noise ratio (S/N), where the relatively large "noises" come from surface roughness, laser beam positioning error and measurement error. From experimental analysis, the standard deviation of surface roughness is around $14\mu m$, the magnitude of laser beam positioning error is $\pm 25\mu m$ and the magnitude of CMM measurement error is $\pm 2\mu m$. Those errors are of similar magnitude as the shape deviations of parts with small size.

Since it is important to conduct independent assessment of shape deviation by excluding surface roughness, we will use this set of experimental data to demonstrate the proposed methods. For parts with larger size, the developed methods and procedures can be applied in the same manner.

3.3 Filtering Surface Roughness

Surface roughness in LPBF is determined by different factors [39]. The out-of-plane roughness is dominated by the stair-step effect, which mainly depends on the powder size and the layer thickness. In-plane roughness, the one of interest in this study, is mainly affected by process parameters, the material properties and the powder size. An as-build average roughness, R_a in the order of 8-12μm was reported for LPBF of steel powders by using default process parameters [39, 40]. Depending on the surface functionality, post-process treatments and machining operations are usually applied to comply with final product specifications. However, to determine the in-plane geometric error of as-build parts, the effect of surface roughness needs to be quantified and taken into account. In our experiment, the roughness measurement is conducted on the circumference of a cylinder with a touch probe profilometer. The roughness profile and measured roughness indexes are reported in Figure 7 and Table 4.

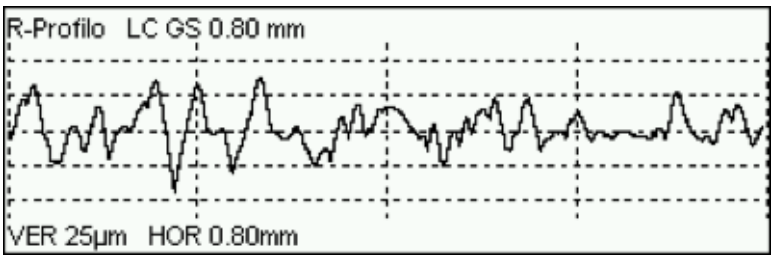

Figure 7: *Measured surface roughness profile for cylinder with* $r_0 = 5mm$

Table 4: *Surface roughness indexes for cylinder with* $r_0 = 5mm$

R_a	R_q	R_z	R_{max}
$10.9\mu m$	$14.2\mu m$	$60.2\mu m$	$80.5\mu m$

where $R_a = \frac{1}{n}\sum_{i=1}^{n}|y_i|$ is the arithmetic average of absolute values, $R_q = \sqrt{\frac{1}{n}\sum_{i=1}^{n}y_i^2}$ is the root mean squared value, R_z is the average maximum height of the profile, R_{max} is the maximum roughness depth and y_i is the roughness value at ith point.

Comparing the measured deviation (dots in Figure 3) and the roughness measurement (Figure 7 and Table 4), the surface roughness is non-negligible. The mixture of roughness dramatically increases the variance of deviation profile, leading to much wide predictive intervals. Therefore, the variance caused by surface roughness needs to be filtered out to achieve actual predictive intervals on shape deviations.

Surface roughness and high frequency components of shape deviations are hard to be distinguished. Considering their distinct characteristics and mechanisms, we introduce two independent components in model error term $\epsilon_\theta \sim N(0, \sigma^2)$ with $\sigma^2 = \sigma_1^2 + \sigma_2^2$. Here σ_1^2 and σ_2^2 are related to shape deviations and surface roughness, respectively. We set σ_2 equal to R_q ($R_q = 14.2\mu m$ in our test part) and leave σ_1 for model estimation from the data.

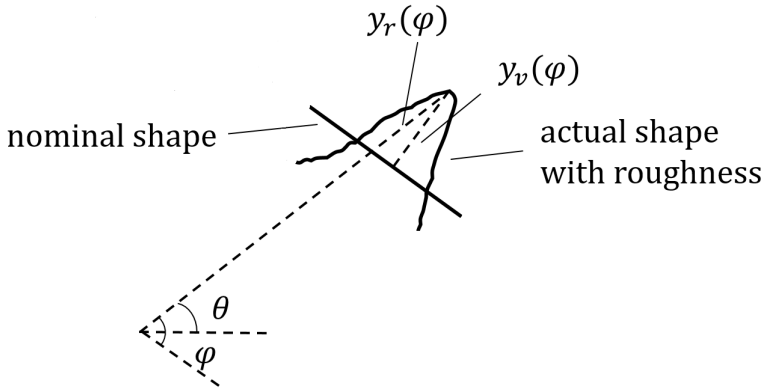

Figure 8: *Illustration of roughness influence in PCS*

One critical issue is that surface roughness is evaluated along the direction normal to the surface, while shape deviations of non-cylindrical surfaces are represented as the deviation along the radial direction under a PCS. Figure 8 shows these two directions are not necessarily parallel to each other. Denote $y_v(\varphi)$ as the measured roughness along the direction normal to the surface. Its impact on shape deviation along the radial direction is $y_r(\varphi) = \frac{y_v(\varphi)}{sin\varphi}$ where φ is the angle with reference parallel to the nominal surface. Translation from θ to φ

is shown in Eq. 6 which is edge-dependent. Therefore in deviation modeling, σ_2 should vary with φ and follow $\sigma_2(\varphi) = \dfrac{\sigma_2}{sin\varphi}$ and

$$\varphi = \theta - \phi_0 + \frac{(n-2)\pi}{2n} + (\frac{2\pi}{n})(\theta - \phi_0)INT(\frac{2\pi}{n}), \quad \theta \in [0, 2\pi] \tag{6}$$

3.4 Initial Model Building and Validation by Filtering Surface Roughness

In this section, we re-establish the shape deviation model by filtering the surface roughness σ_2. We use the same dataset and model estimation procedure introduced in Section 3.1.

The Bayesian model estimation of cylindrical basis model Eq. 2 and the whole freeform model Eq. 1 are listed in Tables 5 and 6, separately. Their corresponding prediction profiles are shown in Figure 9 and 11, while the 2.5%, mean and 97.5% posterior quantiles consider σ_1 only. Apparently, considering surface roughness in model fitting greatly improve the prediction power for shape deviations.

Table 5: *Summary of posterior draws in cylindrical model*

	Mean	SD	2.5%	Median	97.5%
β_0	-0.002118	6.2380×10^{-4}	-0.003185	-0.002157	-0.000851
β_1	-0.001067	4.2940×10^{-4}	-0.002067	-0.001034	-0.000382
a	0.763537	0.098170	0.624365	0.743364	1.012372
b	0.841486	0.156348	0.587817	0.830261	1.160492
x_0	0.006113	0.001427	0.003129	0.006126	0.008806
σ_1	0.002675	0.001813	6.8206×10^{-4}	0.002923	0.005676

Table 6: *Summary of posterior draws for estimating freeform model*

	Mean	SD	2.5%	Median	97.5%
β_0	-0.001614	6.9346×10^{-5}	-0.001752	-0.001612	-0.001490
β_1	-7.0420×10^{-4}	6.5672×10^{-5}	-8.2621×10^{-4}	-7.0442×10^{-4}	-5.7230×10^{-4}
β_2	-5.5815×10^{-4}	3.5792×10^{-4}	-0.001193	-4.6014×10^{-4}	-1.0681×10^{-4}
α	1.45006	0.295512	1.042592	1.426695	1.987236
σ_1	0.010975	4.9288×10^{-4}	0.009997	0.010974	0.011985

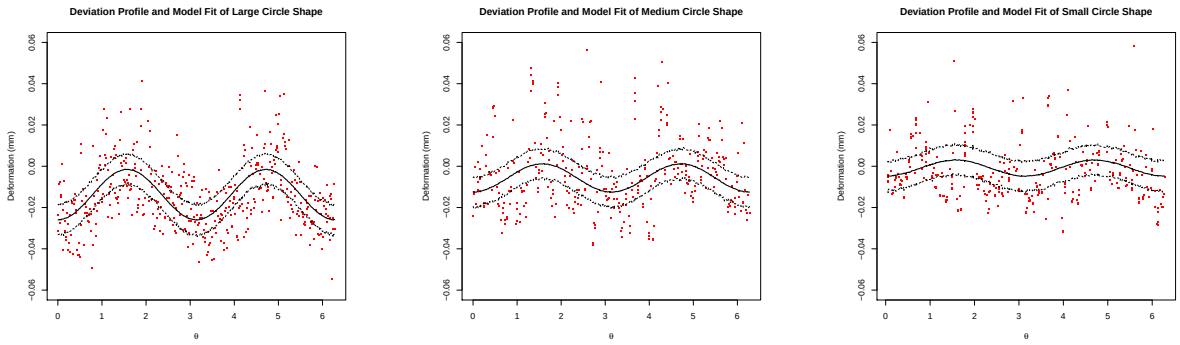

(a) 20*mm cylinder* **(b)** 10*mm cylinder* **(c)** 5*mm cylinder*

Figure 9: *Actual deviation (dots) and prediction profiles (solid lines denote posterior means, and dashed lines denote the* 2.5% *and* 97.5% *posterior quantiles) of three cylinders by cylindrical basis model* g_1 *while filtering surface roughness*

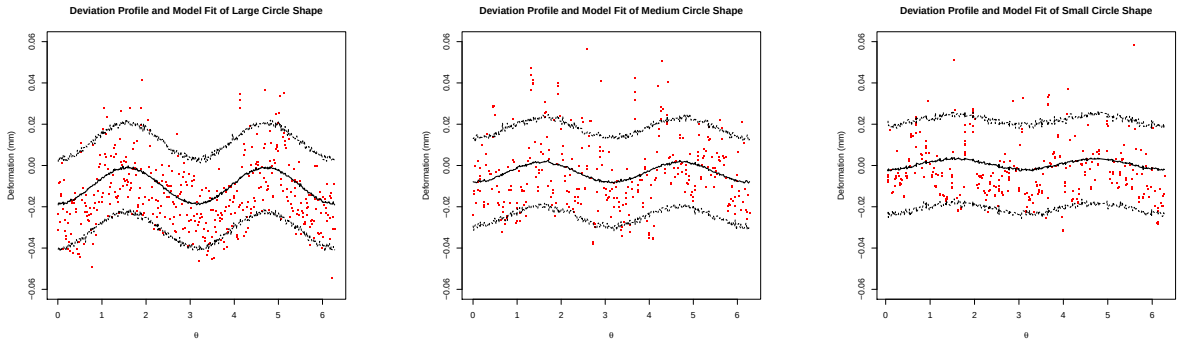

(a) 20*mm cylinder* **(b)** 10*mm cylinder* **(c)** 5*mm cylinder*

Figure 10: *Actual deviation (dots) and prediction profiles (solid lines denote posterior means, and dashed lines denote the* 2.5% *and* 97.5% *posterior quantiles) of three cylinders by freeform model while filtering surface roughness*

Applying the estimated parameters to the generalized freeform model (Eqs. 1, 4, 5), the predicted shape deviation profile of the freeform shape after filtering the surface roughness is shown in Figure 12.

Figures 10, 11 and 12 still indicate 95% predictive intervals that contain the zero line, meaning the null hypothesis of no geometric shape deviation still cannot be rejected. The major reason is that besides surface roughness, other "noises" such as laser beam positioning error and measurement error are still relatively large comparing to the small size of experimental parts, making the signal to noise ratio (S/N) still relatively low.

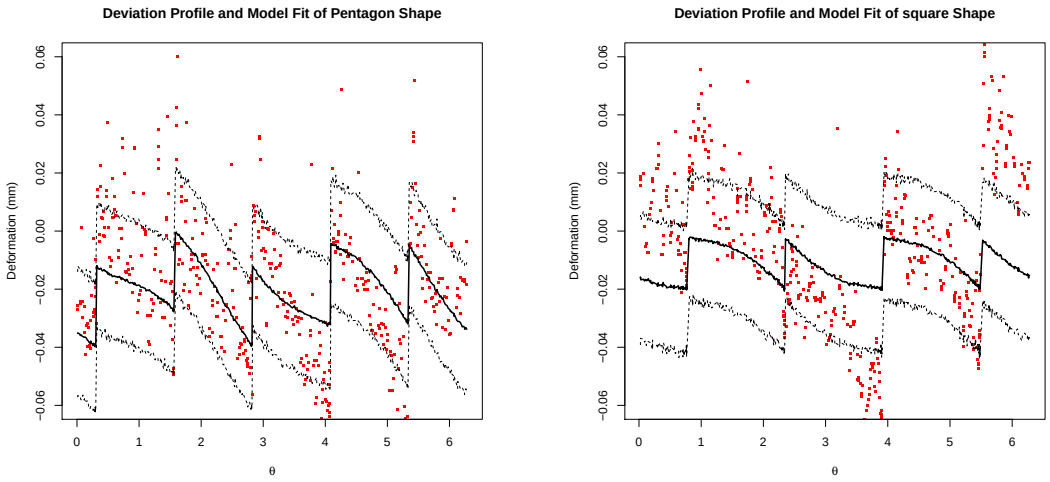

(a) $15mm$ *pentagon* **(b)** $13\sqrt{2}mm$ *square*

Figure 11: *Actual deviation (dots) and prediction profiles (solid lines denote posterior means, and dashed lines denote the* 2.5% *and* 97.5% *posterior quantiles) of the polyhedron shapes by freeform model while filtering surface roughness*

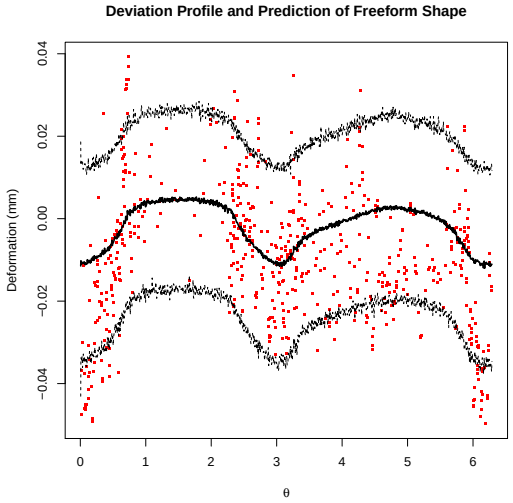

Figure 12: *Actual deviation profile (dots) and prediction (solid lines denote posterior means, and dashed lines denote the* 2.5% *and* 97.5% *posterior quantiles) of* 12mm *freeform shape while filtering surface roughness*

4 Laser Beam Positioning Error Prediction and Elimination with Error Equivalence Concept

Quality of AM built parts can vary with spatial locations on a building plate. Laser beam positioning error and other machine-dependent location effects are two influential sources

contributing to spatial variations. In this section, we will first introduce the location-effect experimentation to investigate these two error sources. Laser beam positioning error will be modeled and integrated into shape deviation prediction. Other location effects will be analyzed in the next Section.

4.1 Location Effect Experimentation

To gain insight into the laser positioning accuracy, a regular grid plate with 9×9 small cylinders are printed by the same LPBF machine (as shown in Figure 13). The radius of each cylinder is $2.5mm$ and the height is $5mm$. The cylinders are produced by using the same process settings and same metal powder described in Section 3.1. The same CMM system with 1mm radius probe is used to measure the circumference profile of cylinders at the height of 4.5mm above the baseplate.

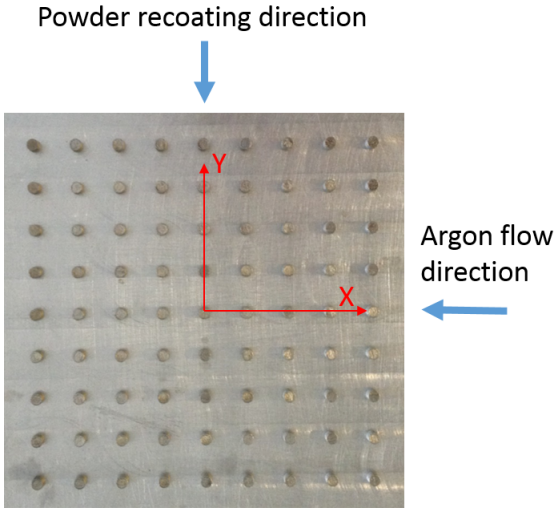

Figure 13: *Experimental grid with* 9×9 *small cylinders in location effect experimentation*

This experimentation is employed to model and predict the two location-dependent errors. The laser beam positioning error is benchmarked by the difference between the actual center of each cylinder and its nominal center, while the machine-dependent location effect at each cylinder location is estimated from each deviation profile.

Since no extra marker is added to locate the part center, the center of each cylinder

needs to be identified via numerical approximation. A linear least square based circle fitting algorithm is adopted here to estimate the actual cylinder center according to CMM measurement data [41]. This algorithm is not sensitive to outliers and provides a quite reliable center estimation for the regular geometries.

4.2 Predictive Modeling of Laser Beam Positioning Error

In the location effect experimentation, the cylinders are so small that their positions are highly influenced by the laser beam positions. Therefore, the actual center of each cylinder could be benchmarked by its nominal position to represent the laser beam positioning error at different locations. The pattern of positioning error within the building area is shown in Figure 14. It shows that the actual laser beam positions tend to be closer to plate center, which is consistent with the analysis of extruder position errors in FDM process [28, 29].

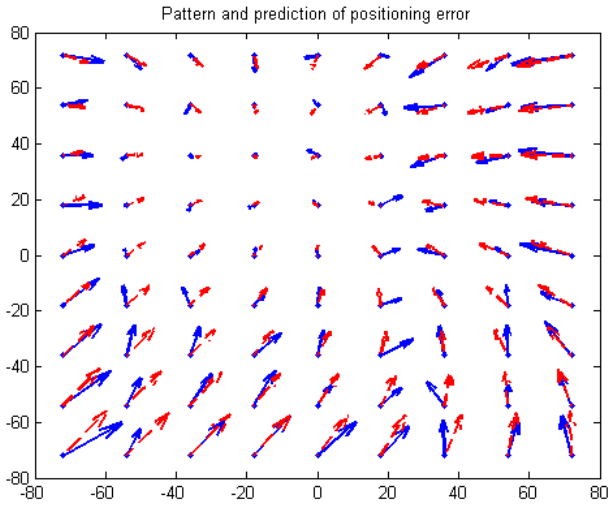

Figure 14: *Pattern of the laser beam positioning error. Each point denotes the desired position of cylinder center. Measured and predicted positioning errors are denoted by solid and dashed arrows, respectively*

The measured laser beam positioning error along $x-$ and $y-$ directions separately are shown as the points in Figure 15. We adopt a 2nd order polynomial model under the assumption of lack of spatial correlation of the residual in Eq. 7 to model the laser beam

positioning error in $x-$ and $y-$ directions separately.

$$Z(x,y) = p_{00} + p_{10} * x + p_{01} * y + p_{20} * x^2 + p_{11} * x * y + p_{02} * y^2 + \epsilon, \epsilon \sim N(0,\sigma) \qquad (7)$$

where $Z(x,y)$ represents either $e_x(x,y)$ or $e_y(x,y)$.

Model estimation as well as 95% confidence interval are listed in Table 7. To verify the existence of laser beam positioning error in both directions, F test with 5 and 75 degrees of freedom is conducted. The small $p-$value for F test indicates the existence of positioning error in both directions. We adopt the sum of square error (SSE) and adjusted R-square to quantify the goodness of fitting, which could be found in Table 8. Corresponding modeling fitting plots and residual plots are shown in Figure 15 and Figure 16. The dashed arrows in Figure 14 show the prediction of positioning error.

Table 7: *Summary of model fitting for positioning errors in $x-$ and $y-$ directions with 95% confidence interval*

	$e_x(x,y)$			$e_y(x,y)$		
	Mean	2.5%	97.5%	Mean	2.5%	97.5%
p_{00}	2.359 $\times 10^{-4}$	-0.003575	0.004047	0.00671	0.004665	0.008756
p_{10}	-2.497 $\times 10^{-4}$	-2.93 $\times 10^{-4}$	-2.065 $\times 10^{-4}$	-8.804$\times 10^{-6}$	-3.201e$\times 10^{-5}$	1.44$\times 10^{-5}$
p_{01}	-1.453 $\times 10^{-4}$	-1.886 $\times 10^{-4}$	-1.021 $\times 10^{-4}$	-2.722 $\times 10^{-4}$	-2.954 $\times 10^{-4}$	-2.49 $\times 10^{-4}$
p_{20}	-1.02 $\times 10^{-6}$	-2.081$\times 10^{-6}$	3.961$\times 10^{-8}$	7.069$\times 10^{-7}$	1.38$\times 10^{-7}$	1.276$\times 10^{-6}$
p_{11}	-9.501 $\times 10^{-7}$	-1.880$\times 10^{-6}$	-1.995$\times 10^{-8}$	-9.936$\times 10^{-8}$	-5.986$\times 10^{-7}$	3.999$\times 10^{-7}$
p_{02}	1.333$\times 10^{-6}$	2.733$\times 10^{-7}$	2.393$\times 10^{-6}$	5.038$\times 10^{-7}$	-6.516$\times 10^{-8}$	1.073$\times 10^{-6}$

Table 8: *Goodness of fitting for positioning error in $x-$ and $y-$ directions*

	$e_x(x,y)$	$e_y(x,y)$
SSE	0.00618	0.00178
Adjusted R-square	0.6997	0.8732
p-value of F test	$< 2.2 \times 10^{-16}$	$< 2.2 \times 10^{-16}$

Since in our experiment, the centers are identified by numerical approximation [41], the measured laser beam positioning error at each cylinder center may contain two portions: the center fitting error and actual positioning error. Consequently, the center fitting error needs to be quantified.

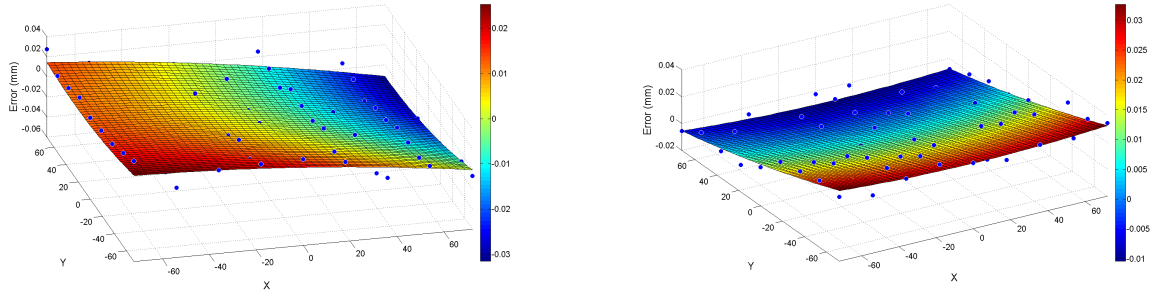

(a) *x− direction* **(b)** *y− direction*

Figure 15: *Measurement (points) and prediction profiles (surface) of the laser beam positioning error (unit: mm)*

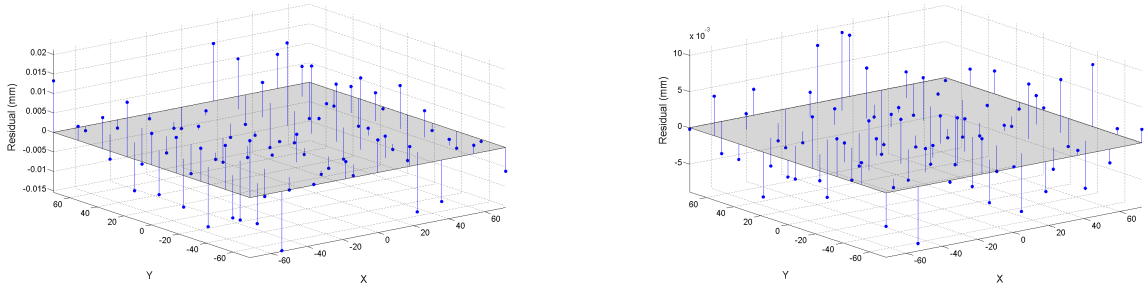

(a) *x− direction* **(b)** *y− direction*

Figure 16: *Model fitting residual plots of the laser beam positioning error (unit: mm)*

Here we adopted a numerical method to estimate the standard deviation of center fitting in both $x-$ and $y-$ directions. For each small cylinder, the measurement data contains around 200 points along the boundary. We randomly pick 160 points for center fitting and repeat 50 times. Figure 17 presents the standard deviation of the 50 estimations for each cylinder. Comparing to the measured positioning error in Figure 15, the center fitting error is negligible. So we will not consider the center fitting error when modeling laser beam positioning error.

4.3 Transforming Positioning Error into the Equivalent Amount of Shape Design Error

In this sub-section we aim to model the impact of laser beam positioning errors on shape deviation. Similar to the extruder positioning error in FDM process [28, 29], the proposed

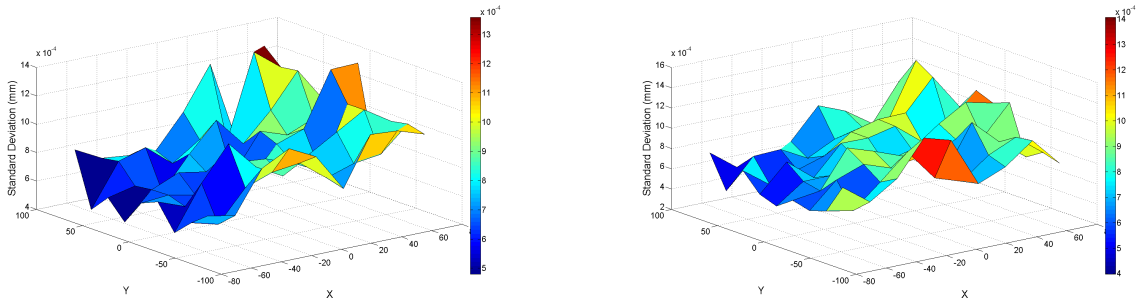

(a) *x− direction* **(b)** *y− direction*

Figure 17: *Center fitting standard deviation of each cylinder (unit: mm)*

strategy of controlling laser beam positioning error is to transform it into the equivalent amount of shape design error. After the transformation, our compensation framework could be able to compensate the positioning error along with the shape deviations.

Laser beam during printing process may deviate from its intended position (x, y) by error $(e_x(x, y), e_y(x, y))$. As a result, the actual point position (x', y') could be presented as:

$$\begin{cases} x' = x + e_x(x, y) \\ y' = y + e_y(x, y) \end{cases} \tag{8}$$

The error equivalence concept [35–38] is adopted to transform positioning error into the equivalent amount of shape design error by:

(i) predicting the actual laser beam position (x', y') with Eq. 8;

(ii) transforming (x', y') into PCS as $r'(\theta)$, then calculating deviation error as $\Delta r(\theta) = r(\theta) - r'(\theta)$.

Here $r(\theta)$ and $\Delta r(\theta)$ represent the actual size and deviation along radius direction at angle θ respectively. Our compensation framework is built to compensate $\Delta r(\theta)$, which contains both shape deviation and positioning error.

Applying the transformed positioning error to the three cylinders in shape deviation experimentation, the equivalent amount of deviation profile containing both actual shape deviation and positioning error is shown in Figure 18. Since the null hypothesis of no

geometric shape deviation cannot be rejected in Section 3, here we will not re-estimate the shape deviation model again.

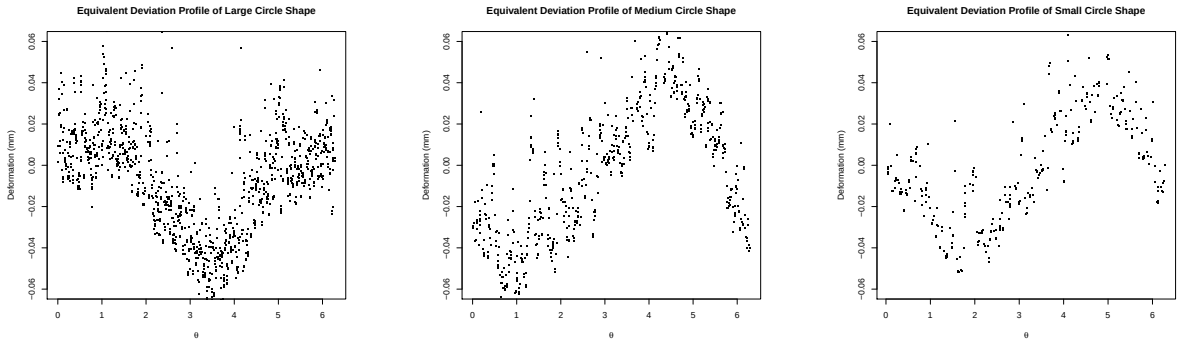

(a) 20*mm cylinder* **(b)** 10*mm cylinder* **(c)** 5*mm cylinder*

Figure 18: *Equivalent deviation profiles of three cylinders*

5 Analysis and Modeling of Additional Location Effects

Different LPBF systems may exhibit different location effects on the resulting geometrical accuracy. This can be caused by difference in the chamber equipment and environmental control configurations. As an example, non uniform inert gas flows may lead to non-uniform shape deviation profiles within the building area. In this study, the existence of additional location effects is approximated as a fixed effect at each location. We adopt the error equivalence concept and use a location-dependent term $x_0(s)$ to capture this effect at location s. Here we use the position of part center $s = (x, y)$ to represent the part location. Termed as the "location effect term", it is represented as the equivalent amount of shape design error, which is integrated as a term into the finalized shape prediction model Eq. 1. Similar treatment can be found for "over-exposure" effect in SLA processes [19].

5.1 Estimation of Location Effect Term $x_0(s)$ at Different Locations

To gain insight of any possible machine-dependent location effect, the actual deviation profiles of the small cylinders in location effect experiment (Figure 13) are analyzed first. For instance, Figure 19 presents the deviation profiles of the 9 cylinders in the top row. Comparing all the deviation profiles, two conclusions could be derived: (i) deviation profiles of those cylinders share the same pattern with our validated shape deviation model; (ii) the deviation magnitudes are slightly different especially in some columns.

We adopt the cylindrical basis model Eq. 2 and the three cylinders ($r = 20mm$, $10mm$, and $5mm$) in shape deviation experiment plus the 81 small cylinders ($r = 2.5mm$) in location effect experiment to estimate $x_0(s)$ at different locations. To gain an estimation consistent with the previously validated model, we fix all the parameters in Table 5 except x_0 and σ_1, then conduct same Bayesian procedures to estimate the 84 independent x_0 simultaneously. The estimated $x_0(s)$ at the 81 locations in location effect experiment is shown as the points in Figure 20a, which verifies that a more severe location effect, possibly cause by a non-uniform gas flow indeed exist at the right top area of the plate.

5.2 Predictive Modeling of Location Effect Term $x_0(s)$

The 81 x_0 estimated by the small cylinders in the location effect experiment are employed to fit the predictive model for $x_0(s)$. The three larger cylinders in shape deviation experiment remain for validation. We still employ a 2nd order polynomial model to predict $x_0(s)$ at any position $s = (x, y)$, which could be formulated as:

$$x_0(s) = p_{00} + p_{10} * x + p_{01} * y + p_{20} * x^2 + p_{11} * x * y + p_{02} * y^2 + \epsilon, \epsilon \sim N(0, \sigma) \qquad (9)$$

Model estimation as well as 95% confidence interval are listed in Table 9. The p-value of F test with 5 and 75 degrees of freedom (shown in Table 10) further illustrate the existence

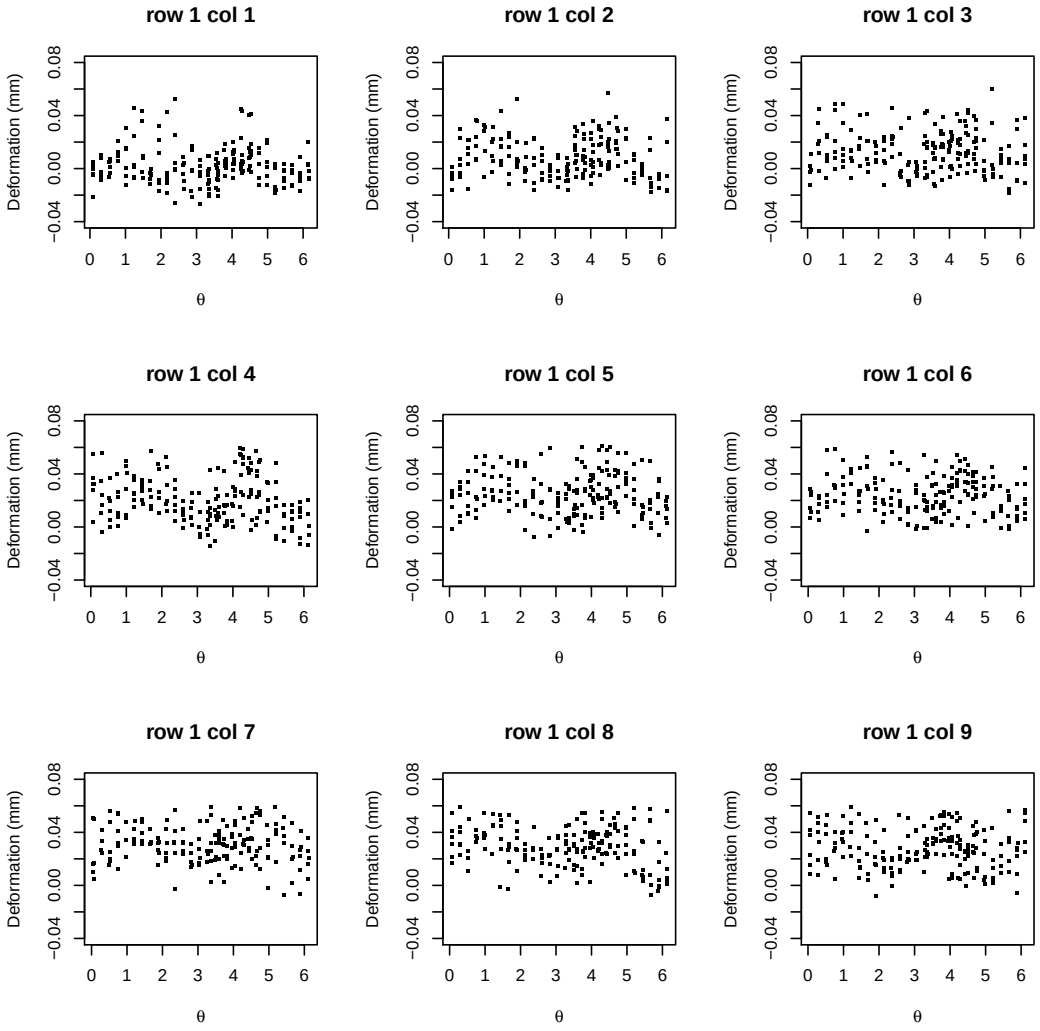

Figure 19: *Deviation profiles of the 9 cylinders in the top row of the grid in location effect experimentation*

of location effect. The sum of square error (SSE) and adjusted R-square are shown in Table 10 to quantify the goodness of fitting. Figure 20 presents the corresponding modeling fitting plots and residual plots.

Validation analysis is conducted on the three cylinders in the shape deviation experiment (Figure 2). The original x_0 fitted when estimating shape deviation model in Section 3.4, the new x_0 fitted when estimating $x_0(s)$ at different locations in Section 5.1 as well as the x_0 predicted by the established model in Eq. 9 are compared in Table 11. The desired center position $s = (x, y)$ of each cylinder is also listed in the table.

Table 9: *Summary of model fitting for location effect term $x_0(s)$ with 95% confidence interval*

	$x_0(s)$		
	Mean	2.5%	97.5%
p_{00}	0.02502	0.02406	0.02597
p_{10}	1.416×10^{-4}	1.308×10^{-4}	1.525×10^{-4}
p_{01}	6.331×10^{-5}	5.244×10^{-5}	7.419×10^{-5}
p_{20}	-1.257×10^{-6}	-1.524×10^{-6}	-9.906×10^{-7}
p_{11}	8.097×10^{-7}	5.758×10^{-7}	1.044×10^{-6}
p_{02}	-3.916×10^{-7}	-6.582×10^{-7}	-1.25×10^{-7}

Table 10: *Goodness of fitting for location effect term $x_0(s)$*

	$x_0(s)$
SSE	0.0003908
Adjusted R-square	0.9221
p-value of F test	$< 2.2 \times 10^{-16}$

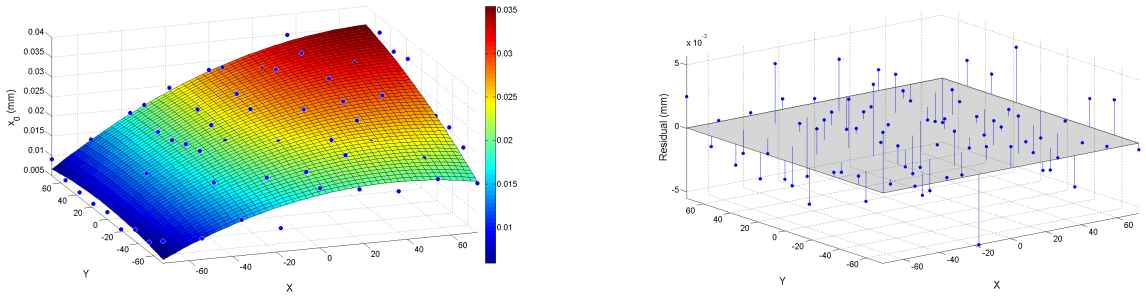

(a) *Estimated $x_0(s)$ (points) and prediction profile (surface)*

(b) *Model fitting residual plot*

Figure 20: *Model fitting and residual plots of the location effect term $x_0(s)$ (unit: mm)*

Table 11: *Fitted vs predicted x_0 for the three cylinders in Figure 2 (unit: mm)*

cylinder radius (mm)	x_0 fitted in shape deviation modeling	x_0 fitted when estimating $x_0(s)$	x_0 predicted by the estimated model	x	y
20	0.006113	0.007339	0.0348	55	72.5
10	0.006113	0.008653	0.0175	25	-87.5
5	0.006113	0.004668	0.0184	75	-67.5

The fitted x_0 are similar no matter being treated as a constant or independent parameters. However, the predicted x_0 is relatively larger than the actual estimated x_0. The reason mainly comes from the lack of data. Although the location effect term x_0 is fixed among different parts, it has a relative higher influence on the small parts. Therefore, if all the parts are very small, the estimation process will pay more weights on $x_0(s)$, leading to some bias. To avoid

the bias, multiple parts with different size should be printed at each location and estimated together.

6 Conclusion

Facing new challenges in the final part quality improvement of LPBF process, this work proposes a prescriptive data-analytical modeling approach that could decouple different error sources and achieve a comprehensive model to predict shape deviations. Building upon our prescriptive in-plane shape deviation modeling and compensation framework for freeform shapes in stereolithography process, this work achieves methodological extension from the following three aspects. First, the non-negligible surface roughness is filtered out from the geometric deviation profile to guarantee confident part deviation prediction. Second, we establish spatial models to quantify laser beam positioning error in both $x-$ and $y-$ directions. Last, we estimate a machine-dependent location effect and build a predictive model. Both the laser beam positioning error and this additional location effect are transfered into equivalent shape design error following equivalent error concept and compensated along with geometric deviation.

The prescriptive shape deviation model is established by using only a limited number of benchmark geometries and validated on a freeform product. The analysis and modeling of the location-dependent errors including laser beam positioning error and machine-dependent location effects are conducted on a 9×9 regular cylinder grid. The modeling analysis demonstrates the existence of both errors in LPBF process. The established spatial predictive models illustrate the goodness of fitting.

Our modeling work is based on the assumption that the LPBF process is stable and repeatable. Build-to-build variation and machine-to-variation should be further investigated and evaluated. Though the proposed data-analytical black-box modeling framework can be applicable to the production of other geometries, further experimentation and analysis is

needed to investigate the LPBF process performance when building larger products with more complicated shapes.

References

[1] W. Report, "3d printing and additive manufacturing state of the industry, annual worldwide progress report,," http://wohlersassociates.com/2018report.htm, 2018.

[2] I. Gibson, D. W. Rosen, B. Stucker *et al.*, *Additive manufacturing technologies*. Springer, 2010, vol. 238.

[3] W. J. Sames, F. List, S. Pannala, R. R. Dehoff, and S. S. Babu, "The metallurgy and processing science of metal additive manufacturing," *International Materials Reviews*, vol. 61, no. 5, pp. 315–360, 2016.

[4] E. O. t. Olakanmi, R. Cochrane, and K. Dalgarno, "A review on selective laser sintering/melting (sls/slm) of aluminium alloy powders: Processing, microstructure, and properties," *Progress in Materials Science*, vol. 74, pp. 401–477, 2015.

[5] M. Mani, S. Feng, B. Lane, A. Donmez, S. Moylan, and R. Fesperman, *Measurement science needs for real-time control of additive manufacturing powder bed fusion processes*. US Department of Commerce, National Institute of Standards and Technology, 2015.

[6] G. Tapia and A. Elwany, "A review on process monitoring and control in metal-based additive manufacturing," *Journal of Manufacturing Science and Engineering*, vol. 136, no. 6, p. 060801, 2014.

[7] T. G. Spears and S. A. Gold, "In-process sensing in selective laser melting (slm) additive manufacturing," *Integrating Materials and Manufacturing Innovation*, vol. 5, no. 1, p. 2, 2016.

[8] S. K. Everton, M. Hirsch, P. Stravroulakis, R. K. Leach, and A. T. Clare, "Review of in-situ process monitoring and in-situ metrology for metal additive manufacturing," *Materials & Design*, vol. 95, pp. 431–445, 2016.

[9] M. Grasso and B. M. Colosimo, "Process defects and in situ monitoring methods in metal powder bed fusion: a review," *Measurement Science and Technology*, vol. 28, no. 4, p. 044005, 2017.

[10] D. Thomas, "The development of design rules for selective laser melting," Ph.D. dissertation, University of Wales, 2009.

[11] B. Sharrat, "Non-destructive techniques and technologies for qualification of additive manufactured parts and processes," *no. March*, 2015.

[12] K. Abd-Elghany and D. Bourell, "Property evaluation of 304l stainless steel fabricated by selective laser melting," *Rapid Prototyping Journal*, vol. 18, no. 5, pp. 420–428, 2012.

[13] S. P. Moylan, J. Drescher, and M. A. Donmez, "Powder bed fusion machine performance testing," in *Proc. of the 2014 ASPE Spring Topical Meeting—Dimensional Accuracy and Surface Finish in Additive Manufacturing (Berkeley, CA,)*, vol. 57, 2014.

[14] B. Foster, E. Reutzel, A. Nassar, B. Hall, S. Brown, and C. Dickman, "Optical, layerwise monitoring of powder bed fusion," in *26th International Solid Freeform Fabrication Symposium; Austin, TX*, 2015.

[15] A. Almabrouk Mousa and A. Almabrouk Mousa, "Experimental investigations of curling phenomenon in selective laser sintering process," *Rapid Prototyping Journal*, vol. 22, no. 2, pp. 405–415, 2016.

[16] L. Papadakis, D. Chantzis, and K. Salonitis, "On the energy efficiency of pre-heating methods in slm/sls processes," *The International Journal of Advanced Manufacturing Technology*, vol. 95, no. 1-4, pp. 1325–1338, 2018.

[17] J.-P. Kruth, P. Mercelis, J. Van Vaerenbergh, and T. Craeghs, "Feedback control of selective laser melting," in *Proceedings of the 3rd international conference on advanced research in virtual and rapid prototyping*, 2007, pp. 521–527.

[18] E. Yasa, J. Deckers, T. Craeghs, M. Badrossamay, and J.-P. Kruth, "Investigation on occurrence of elevated edges in selective laser melting," in *International Solid Freeform Fabrication Symposium, Austin, TX, USA*, 2009, pp. 673–85.

[19] Q. Huang, J. Zhang, A. Sabbaghi, and T. Dasgupta, "Optimal offline compensation of shape shrinkage for three-dimensional printing processes," *IIE Transactions*, vol. 47, no. 5, pp. 431–441, 2015.

[20] Q. Huang, H. Nouri, K. Xu, Y. Chen, S. Sosina, and T. Dasgupta, "Predictive modeling of geometric deviations of 3d printed products-a unified modeling approach for cylindrical and polygon shapes," in *2014 IEEE International Conference on Automation Science and Engineering (CASE)*. Taipei, Taiwan: IEEE, August 18-22 2014, pp. 25–30.

[21] ——, "Statistical predictive modeling and compensation of geometric deviations of three-dimensional printed products," *ASME Transactions, Journal of Manufacturing Science and Engineering*, vol. 136, no. 6, pp. 061 008–061 018, 2014.

[22] A. Sabbaghi, T. Dasgupta, Q. Huang, and J. Zhang, "Inference for deformation and interference in 3d printing," *Annals of Applied Statistics*, vol. 8, no. 3, pp. 1395–1415, 2014.

[23] A. Sabbaghi, Q. Huang, and T. Dasgupta, "Bayesian additive modeling for quality control of 3d printed products," in *Automation Science and Engineering (CASE), 2015 IEEE International Conference on*. IEEE, 2015, pp. 906–911.

[24] ——, "Bayesian model building from small samples of disparate data for capturing in-plane deviation in additive manufacturing," *Technometrics*, no. just-accepted, 2017.

[25] Q. Huang, "An analytical foundation for optimal compensation of three-dimensional shape deformation in additive manufacturing," *Journal of Manufacturing Science and Engineering*, vol. 138, no. 6, p. 061010, 2016.

[26] H. Luan and Q. Huang, "Predictive modeling of in-plane geometric deviation for 3d printed freeform products," in *Automation Science and Engineering (CASE), 2015 IEEE International Conference on*. IEEE, 2015, pp. 912–917.

[27] ——, "Prescriptive modeling and compensation of in-plane shape deformation for 3-d printed freeform products," *IEEE Transactions on Automation Science and Engineering*, vol. 14, no. 1, pp. 73–82, 2017.

[28] S. Song, A. Wang, Q. Huang, and F. Tsung, "Shape deviation modeling for fused deposition modeling processes," in *Automation Science and Engineering (CASE), 2014 IEEE International Conference on*. IEEE, 2014, pp. 758–763.

[29] A. Wang, S. Song, Q. Huang, and F. Tsung, "In-plane shape-deviation modeling and compensation for fused deposition modeling processes," *IEEE Transactions on Automation Science and Engineering*, vol. 14, no. 2, pp. 968–976, 2017.

[30] Y. Jin, S. J. Qin, and Q. Huang, "Out-of-plane geometric error prediction for additive manufacturing," in *Automation Science and Engineering (CASE), 2015 IEEE International Conference on*. IEEE, 2015, pp. 918–923.

[31] ——, "Offline predictive control of out-of-plane shape deformation for additive manufacturing," *Journal of Manufacturing Science and Engineering*, vol. 138, no. 12, p. 121005, 2016.

[32] ——, "Prescriptive analytics for understanding of out-of-plane deformation in additive manufacturing," in *Automation Science and Engineering (CASE), 2016 IEEE International Conference on*. IEEE, 2016, pp. 786–791.

[33] A. Ladewig, G. Schlick, M. Fisser, V. Schulze, and U. Glatzel, "Influence of the shielding gas flow on the removal of process by-products in the selective laser melting process," *Additive Manufacturing*, vol. 10, no. 1-9, 2016.

[34] A. B. Anwar and Q. C. Pham, "Selective laser melting of alsi10mg: Effects of scan direction, part placement and inert gas flow velocity on tensile strength," *Journal of Materials Processing Technology*, vol. 240, pp. 388–396, 2017.

[35] H. Wang, Q. Huang, and R. Katz, "Multi-operational machining processes modeling for sequential root cause identification and measurement reduction," *Journal of manufacturing science and engineering*, vol. 127, no. 3, pp. 512–521, 2005.

[36] H. Wang and Q. Huang, "Error cancellation modeling and its application to machining process control," *IIE transactions*, vol. 38, no. 4, pp. 355–364, 2006.

[37] ——, "Using error equivalence concept to automatically adjust discrete manufacturing processes for dimensional variation control," *Journal of manufacturing science and engineering*, vol. 129, no. 3, pp. 644–652, 2007.

[38] A. Sabbaghi and Q. Huang, "Predictive model building across different process conditions and shapes in 3d printing," in *Automation Science and Engineering (CASE), 2016 IEEE International Conference on*. IEEE, 2016, pp. 774–779.

[39] G. Strano, L. Hao, R. M. Everson, and K. E. Evans, "Surface roughness analysis, modelling and prediction in selective laser melting," *Journal of Materials Processing Technology*, vol. 213, no. 4, pp. 589–597, 2013.

[40] D. Wang, D. Wang, Y. Liu, Y. Liu, Y. Yang, Y. Yang, D. Xiao, and D. Xiao, "Theoretical and experimental study on surface roughness of 316l stainless steel metal parts obtained through selective laser melting," *Rapid Prototyping Journal*, vol. 22, no. 4, pp. 706–716, 2016.

[41] I. D. Coope, "Circle fitting by linear and nonlinear least squares," *Journal of Optimization Theory and Applications*, vol. 76, no. 2, pp. 381–388, 1993.